Perforated Semishells: Far-Field Directional Control and Optical Frequency Magnetic Response

Nikolay A. Mirin,[†,‡,∥] Tamer A. Ali,[†,§,∥] Peter Nordlander,[†,§,⊥] and Naomi J. Halas[†,‡,§,⊥,*]

[†]Laboratory for Nanophotonics (LANP), [‡]Department of Chemistry, [§]Department of Electrical and Computer Engineering, and [⊥]Department of Physics and Astronomy, Rice University, Houston, Texas 77005. [∥]These authors contributed equally to this work.

ABSTRACT Reduced-symmetry plasmonic nanostructures can be designed to support a range of novel optical phenomena, such as nanoscale control of the far-field scattering profile and magnetic resonances at optical frequencies. A family of reduced-symmetry nanostructures—plasmonic semishells with specifically shaped and oriented perforations introduced into the metallic shell layer—can be tailored to control these effects. Unlike core−shell nanoparticles, perforated semishells can be fabricated using a combination of clean-room techniques. For a semishell with a single spherical perforation positioned on its symmetry axis, we examine how the resonant modes of the structure depend on hole size and shape. Placing the perforation off the symmetry axis allows a family of higher-order modes to be excited in the nanostructure, along with complex near-field charge distributions for the various resonant modes. This reduced-symmetry case provides a platform for optical studies, which agree quite well with theoretical analysis. Our study also examines two important variations of this structure: a semishell with multiple perforations in the shell layer, and a semishell with a wedge-like "slice" in the shell layer. A semishell with a wedge-like perforation can be thought of as a three-dimensional analogue of a split-ring resonator (SRR), an important nanoscale component in metamaterial design. Here we show that the dimensions of the wedge-like perforation, which control the effective optical frequency resistance, inductance, and capacitance of this structure, determine the frequency of the magnetic mode.

KEYWORDS: plasmon · symmetry · etching · optical · semishell · magnetism · metamaterial

Metallic nanostructures are a vital component of future optical materials and devices, including metamaterials,[1−6] logic circuits,[7−12] sensors, and energy transducing structures.[13−17] In a metamaterial, the optical response is determined by the geometry of its subwavelength constituents, typically metallic structures, which define the frequency-dependent optical response of the material and its ability to control and manipulate light. As electrical interconnects decrease in size, approaching the fundamental quantum limit, metal plasmonic nanostructures become an alternative to replace conventional on-chip interconnects.[7,18] By focusing light to volumes far below the diffraction limit, plasmonic nanostructures enable subwavelength optical components on the size scale of modern integrated logic circuits.[7,19]

Plasmonic nanostructures can also enhance the conversion of light to electrical energy in solar cells[13,14,16,20] and the conversion of electrical to light energy in light-emitting diodes (LEDs),[21−26] improving energy conversion efficiencies.

The optical response of a plasmonic nanostructure is a sensitive function of its geometry and can be controlled using a range of metal−dielectric geometries, while keeping the overall size small.[27−29] The spatial distribution of the local fields of a plasmonic nanostructure determines its interaction with the surrounding medium. Introducing defects or reducing structure symmetry in a controlled manner can allow for light coupling to plasmon modes whose interaction would otherwise be forbidden. Such symmetry breaking can result in magnetically excited modes,[1−4,6,30] electromagnetically induced transparency,[30] excitation of propagating modes in nanowires[31,32] and thin metal films,[33,34] and localized nanoparticle plasmons.[35−37] Recently, it was shown that reduced symmetry structures[29,38−41] can have a strong structural resonance tunability, large local field enhancements, and strong directionality of scattered light.[14,37] "Nanocups" or semishells are excellent examples of asymmetric plasmonic nanostructures.[37,42−45] The resonances of these partially metal-coated dielectric spheres depend on the size of the dielectric sphere and the thickness of the metal shell layer and, additionally, can be modified by the geometric configuration of the metal edge and its surface roughness.

Here we use a nanocup, or semishell, as our starting point to design and fabricate a family of novel plasmonic nanostructures with interesting and useful properties. By fabricating a perforation into the metallic shell layer of a semishell, its optical

*Address correspondence to halas@rice.edu.

Received for review March 15, 2010 and accepted April 21, 2010.

Published online April 29, 2010. 10.1021/nn100535m

properties can be altered dramatically. We examine the effect of hole size, shape, and location on the optical properties of the nanostructure. We begin by examining a symmetrically placed hole on a semishell, examining the effect of hole size and shape on the optical properties of the perforated semishell. Shifting the perforation to an arbitrary off-axis location on the semishell alters its optical properties, allowing the excitation of a series of higher-order resonances. A fabrication protocol is developed that allows us to access this reduced-symmetry regime experimentally, to probe its optical properties. This approach combines anisotropic metal deposition with anisotropic metal etching on nanoparticles deposited on substrates and is a practical fabrication method for depositing partial metallic shell layers onto nanoparticles in complex configurations and geometries. Finally, we explore two interesting perforated semishell regimes: the case of a semishell with multiple perforations, and the case of a semishell with a wedge-like perforation, which possesses a tunable magnetic plasmon mode suitable for metamaterial applications. We examine how the dimensions of the wedge control the magnetic resonance characteristic of this geometry.

RESULTS AND DISCUSSION

Our initial studies start with the symmetric structure, which consists of an ellipsoidal semishell with a spherical cavity, where the shell thickness gradually decreases from the symmetry axis to the edges of the shell layer. Such a non-uniform thickness gradient provides a realistic model of metallic shell growth using gold evaporation onto spherical nanoparticles that have been immobilized on a substrate.[37,43] In the present study, the inner spherical surface radius is 55 nm and the outer shell radii are 60 nm at the edges and 65 nm at the center of the semishell layer. We start by introducing a circular cylindrical hole into the center of the semishell metallic layer (Figure 1). The evolution of the semishell spectra as a function of the hole radius r from 0 nm (unperforated semishell) to 50 nm is shown in Figure 1A. Two different orientations of incident polarization are examined: where the electric field is polarized along the symmetry axis of the structure and the direction of propagation of light parallel to the edge of the semishell (Figure 1A, left), and the case where the **k**-vector is along the symmetry axis of the nanostructure (Figure 1A, right). We will refer to these two cases as axial and transverse polarization, respectively. For the case of $r = 0$ nm, an unperforated semishell, the structure supports a dipole mode that follows the polarization of the incident light, as the **E**-field of the incident wave drives the electrons in the semishell. Axially polarized incident light excites an axial dipole mode at $\lambda = 832$ nm (Figure 1A, left), and transverse-polarized

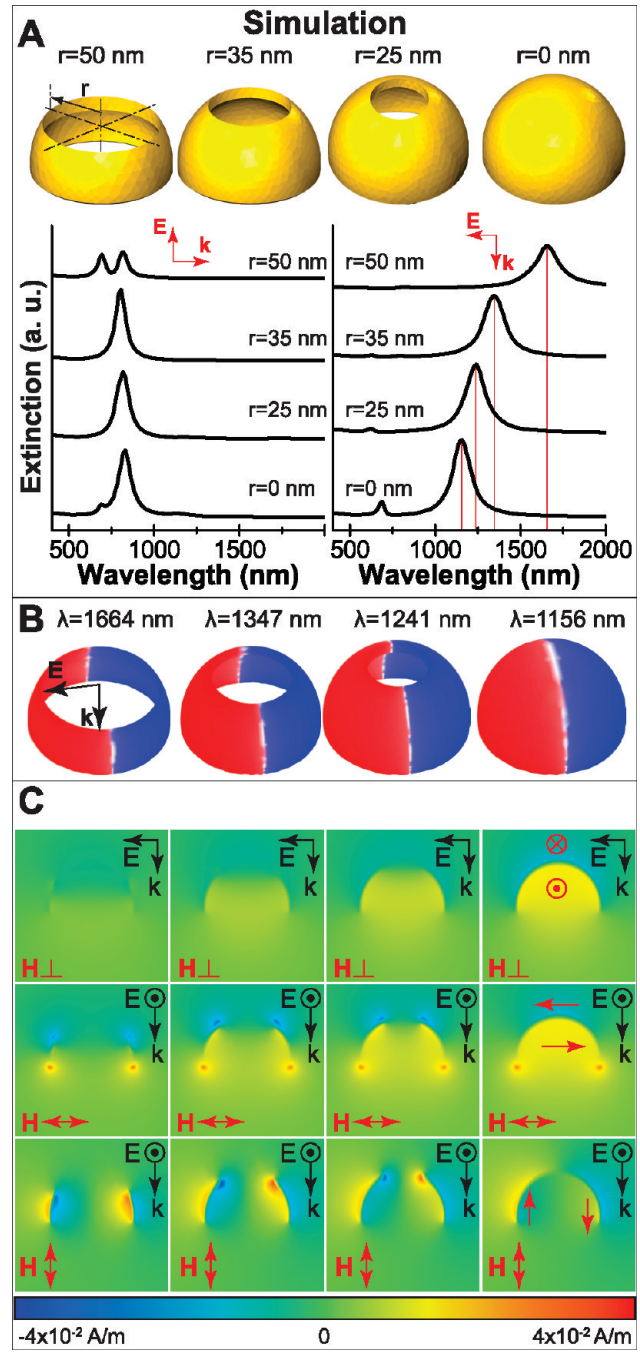

Figure 1. Calculated bright plasmon modes of a semishell of radius r = 65 nm, with a circular cylindrical, coaxial hole, for three hole radii (left to right): r = 50 nm, r = 35 nm, r = 25 nm, and r = 0 nm (for comparison). The same sequence of geometries is calculated in A–C. (A) Schematic of the nanostructure geometry and extinction spectra for plasmon modes excited by axial polarization (left) and transverse polarization (right). (B) Induced electric charge plots for the tunable transverse dipole resonance. (C) Magnetic field enhancements in different directions (red double arrows) for the transverse dipole resonances, showing the reshaping of the field distribution as a function of hole radius.

incident light excites a transverse dipole at $\lambda = 1156$ nm (Figure 1A, right). Weak quadrupolar features are observed at slightly higher energy relative to the dipolar mode in each case.

Introducing a small circular cylindrical perforation on the symmetry axis of the semishell affects the properties of the axial and the transverse modes in different ways. The axial mode (Figure 1A, left) is only slightly blue-shifted with increasing hole radius. This blue shift occurs due to the reduction of the semishell side wall height, which shortens the physical path for the plasmon oscillation and therefore correspondingly increases the energy of the mode. The blue-shifted dipolar plasmon appears to attenuate the weaker quadrupolar plasmon for a large range of hole radii. For very large hole radii, the dipolar mode itself is strongly attenuated due to the decrease in the number of accessible electrons in the thin ring-like structure, and the higher energy quadrupolar mode reappears. For the transverse plasmon, we can conceptualize the introduction of a perforation on the symmetry axis as changing the topology of the structure to a distorted disk, which would yield two hybridized distorted ring modes, a bright "bonding" mode at lower energies and a weak "antibonding" mode at higher energies. Since only the bonding mode contributes appreciably to the optical spectrum of the structure, we focus exclusively on this mode. As the hole radius is increased, the transverse plasmon resonance begins to shift quite strongly to lower energies, particularly when the hole radius approaches half the semishell radius (Figure 1A, right). When the hole radius approaches the semishell radius, the geometry reduces to the case of a nanoring.[46−51]

For the tunable transverse dipole mode, the effect of hole size on the induced surface charge and on the local magnetic field enhancement is shown (Figure 1B,C, respectively). The charge distribution of the transverse resonance shows a strong dipolar character for all hole radii (Figure 1B). In contrast, the local magnetic field distribution is remarkably dependent on the hole size (Figure 1C). For the case of a semishell without a hole (Figure 1C, right), the magnetic field component aligning with the incident magnetic field is enhanced due to the plasmonic current oscillating in the **k**−**E** plane. The net enhanced magnetic field is uniformly distributed inside the semishell. The coaxial hole reduces this enhancement and focuses the magnetic field components into the "hotspots" at the semishell edges. The presence of the circular cylindrical perforation in the semishell alters the resonant plasmonic currents, forcing them to oscillate outside the **k**−E plane. This enhances the local magnetic field components normal to the incident magnetic field around the semishell side walls.

A variation of this structure that is both interesting and relevant for comparison with experimentally fabricated semishell structures is a semishell with an elliptical cylindrical, rather than circular cylindrical, perforation. We consider the case of a symmetrically placed perforation on the semishell, where the shape of the perforation is changed from circular to elliptical (Figure 2). When illuminated at normal incidence, the elliptical hole breaks the azimuthal symmetry of the semishell, splitting the transverse mode into two different energies depending on the polarization of incident light. The optical extinction spectra of a semishell with centered circular and elliptical holes are compared in Figure 2A. The elliptical hole has a major radius $r_{max} = 50$ nm and a minor radius of $r_{min} = 35$ nm (Figure 2A(ii,iii)). It is compared to a semishell with a circular hole of radius $r = 50$ nm (Figure 2A(i)) and a semishell with a circular hole of radius $r = 35$ nm (Figure 2A(iv)), corresponding to the major and minor elliptical hole radii. Here we see a correspondence between the resonances of these structures that at first appears counterintuitive. When the incident polarization is along the minor axis of the ellipse (Figure 2A(ii)), the resonance energy coincides with that of a semishell with a circular hole equal to the size of the major axis (Figure 2A(i)). Similarly, when the incident light is polarized along the major axis of the ellipse (Figure 2A(iii)), the structure has a resonance energy corresponding to a circular hole equal to the dimensions of the ellipse's minor axis (Figure 2A(iv)). This surprising correspondence can be understood by considering that the plasmon resonance energy is determined by the width of the metallic junction and not by the dimensions of the hole or gap.

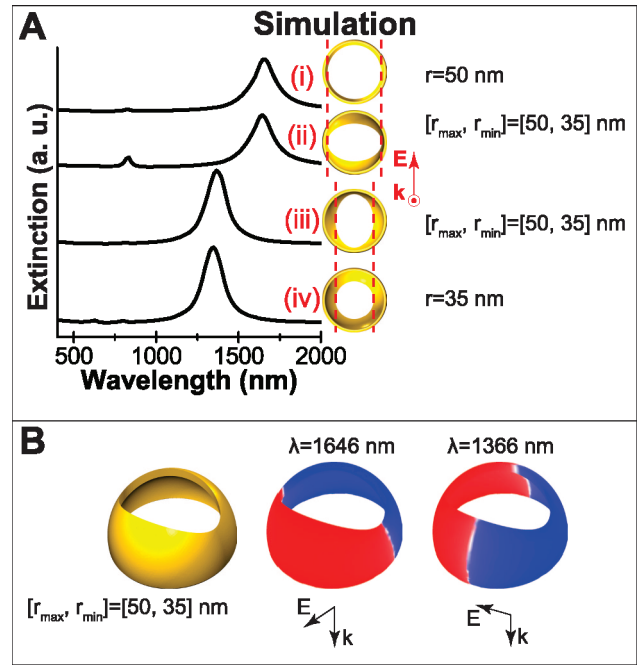

Figure 2. (A) Calculated extinction spectra of a semishell with a coaxial hole: (i) circular cylindrical, $r = 50$ nm; (ii) elliptical cylindrical $[r_{max}, r_{min}] = [50, 35]$ nm, incident polarization along minor axis; (iii) elliptical cylindrical $[r_{max}, r_{min}] = [50, 35]$ nm, incident polarization along major axis; (iv) circular cylindrical, $r = 35$ nm. (B) Induced charge plots for the two transverse dipole modes.

When the polarization is along the minor axis of the elliptical hole, the metallic channel supporting the plasmon oscillation is the same size as for a circular hole of radius 50 nm. Likewise, for incident polarization along the major axis of the elliptical hole, the metallic channel supporting the plasmon oscillation is the same size as for a circular hole of 35 nm radius. This is evident in the charge plots shown in Figure 2B, where the electric charge distribution at the maximal charge separation is shown for both polarizations. Therefore, the optical response of a semishell with an elliptical hole is polarization-dependent, with plasmon energies determined by the hole dimension perpendicular to the direction of polarization.

In addition to the effect of hole size and shape, the position of the hole on the semishell also plays an important role in controlling the optical response. The geometry of a semishell with a circular cylindrical hole of radius $r = 30$ nm shifted away from the symmetry axis of the structure is shown in Figure 3A. The parameter describing the hole offset is the angle β between the rotational axis of the semishell and the axis of the hole (Figure 3A). This structure is no longer azimuthally symmetric, and the optical response is determined by the hole offset. Two topologically different structures are shown in Figure 3A. For $\beta \leq 60°$, the hole does not intersect the semishell edge and overlaps the semishell completely. For $\beta = 90°$, only 50% of the hole area overlaps the semishell.

The calculated extinction spectra are shown in Figure 3. Three sequences of spectra for increasing polar angle of displacement of the hole from the center of the semishell are shown. For incident light propagating along the symmetry axis of the semishell, two polarizations, where the hole displacement is in the **k**−**H** plane (Figure 3B) and where the hole displacement is in the **k**−**E** plane (Figure 3C), are shown. Figure 3D shows the spectra for polarization along the symmetry axis of the semishell. The presence of the hole modifies the topology of the structure, allowing plasmon oscillations between the hole and the cup edges. The position of the hole determines the strength of the coupling to the incident light.

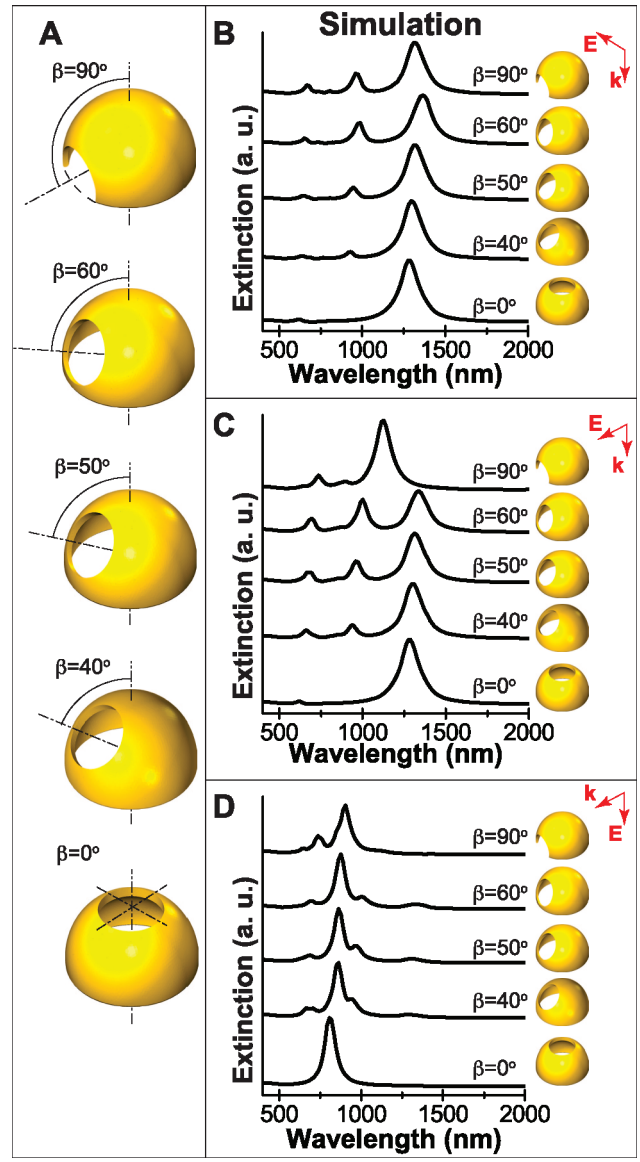

Figure 3. Effect of cylindrical ($r = 30$ nm) nonaxial holes on the semishell optical extinction spectra. (A) Schematic of the semishell geometry for holes positioned at increasing offset angles from the symmetry axis of the semishell. (B) Extinction spectra as a function of hole offset in k−H plane with coaxial k-vector of incident light. (C) Extinction spectra as a function of hole offset in k−E plane with coaxial k-vector of incident light. (D) Extinction spectra as a function of hole offset in k−E plane with k transverse and E coaxial to the cup.

The semishell with an off-axis hole provides key information about the origin of the plasmon modes of perforated semishells. For the transverse **E**-field polarization case (Figure 3B,C), the spectra are dominated by the longer wavelength (~1300 nm) dipole mode: this is the same "tunable" mode shown in Figure 1A (right) and in the charge distributions in Figure 1B for the hole with a radius $r = 35$ nm. Here we see that the major effect of the hole offset is the enabling of higher-order plasmon excitation (Figure 3B,C). Here we observe that the relative intensities of the higher and lower-order modes are determined by the position of the hole. Large hole offsets correspond to stronger intensities of higher-order modes. In contrast, for the case of axial polarization (Figure 3D), the spectra are only weakly dependent on the hole offset from the symmetry axis.

These spectral characteristics can be well-understood by examining the charge distributions of the plasmon modes. Without a perforation, electrons in the semishell oscillate between the primary edges of the semishell structure, as driven by the **E**-field of the incident light at resonance. The presence of a perfora-

tion modifies the path for the electrons oscillating between the primary edges of the semishell structure, forcing the resonant currents to circumvent the perforation. For the case of the coaxial hole ($\beta = 0°$), the oscillating dipoles on either side of the semishell are collinear, and only the in-phase bonding mode is observed (Figure 1B). When the hole is shifted from the symmetry axis (Figure 3A, $0° < \beta \leq 60°$), the dipoles on the hole edges are no longer collinear and both bonding and antibonding modes have nonvanishing dipoles (Figure 4A,B). The most pronounced low energy (~1300 nm) resonance corresponds to the dipole bonding mode case in which the induced dipolar charges oscillate in phase on both edges (Figure 4A, $\lambda =$ 1338 nm). The magnetic field enhancement of this mode (Figure 4B) is perturbed by the hole in the same manner as in Figure 1C. The next resonance (Figure 4A, $\lambda = 1002$ nm) corresponds to an antibonding mode where the same dipoles oscillate in opposite phases. The shortest wavelength mode (Figure 4A, $\lambda = 694$ nm) corresponds to quadrupolar charge distributions on the semishell and hole edges. The antibonding and quadrupolar modes become visible in the spectra of the symmetry-broken structures because of the hybridization with the dipolar semishell mode.

When the perforation intersects with the semishell edge (Figure 3A, $\beta = 90°$), the structure no longer has two distinct edges and its spectral response changes qualitatively in a polarization-sensitive manner (Figure 4C,D). This topology is equivalent to a semishell with an edge defect, a structure which also supports higher-order modes. The higher-order modes are modified semishell modes (Figure 4C) in which higher-order charge distributions can be optically excited, due to the dipole moment acquired from the surface charges along the edge defect. This also results in enhanced local magnetic fields (Figure 4D).

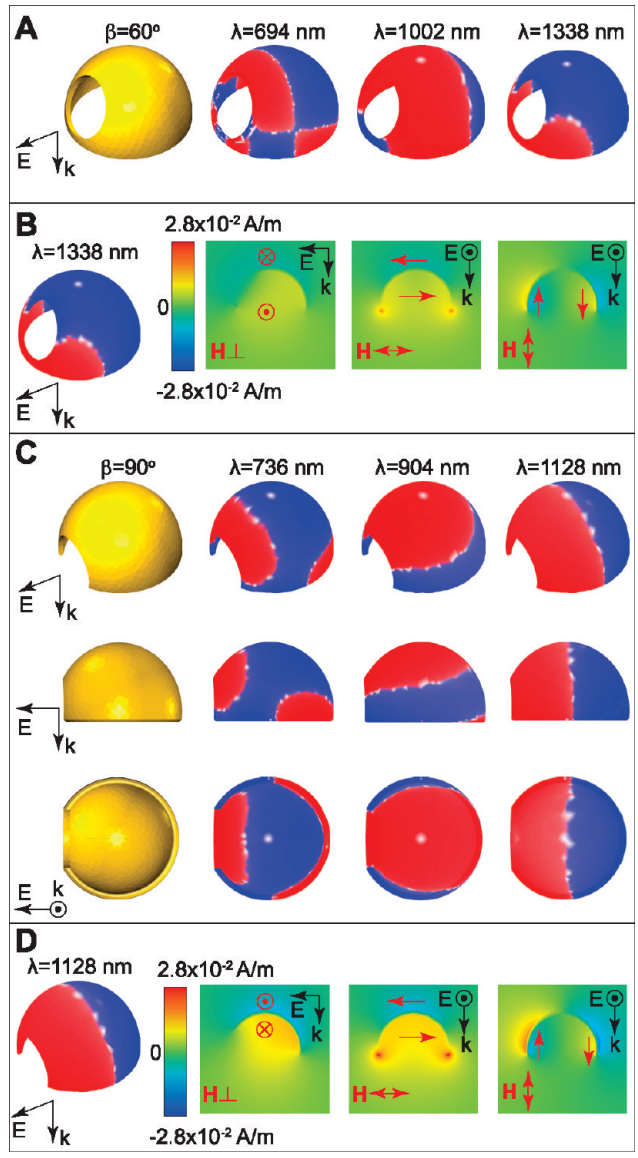

Figure 4. Effect of cylindrical ($r = 30$ nm) nonaxial holes on the semishell induced charge distribution and local magnetic field enhancement. (A) Induced charge distribution of the plasmonic modes for the case of a nanocup with a hole near the edge: quadrupolar charge distribution ($\lambda = 694$ nm), opposite dipoles on semishell and hole edges ($\lambda = 1002$ nm), same phase dipoles on semishell and hole edges ($\lambda =$ 1338 nm). (B) Magnetic field enhancement for the dipole mode of the semishell with a hole near the edge. (C) Induced charge distribution of plasmonic modes for the case of a semishell with a hole intersecting its edge, showing dipolar ($\lambda = 1128$ nm) and quadrupolar ($\lambda = 736$ and 904 nm) modes. (D) Magnetic field enhancement for the dipole mode of a semishell with a hole intersecting the edge.

We have developed a straightforward fabrication protocol for perforated semishells by extending our previously reported method of semishell fabrication,[37] including an etching process previously used for the semishell[45] and nanocrescent[52] fabrication. The fabrication steps are shown schematically in Figure 5, with a more detailed description in the Methods section. Six different structures were fabricated, using evaporation angles of 30 and 45° (Figure 5B) with 0, 30, and 45 s etching times (Figure 5C). Each sample was imaged using scanning electron microscopy (SEM). Representative images for both deposition angles and all etch times are shown in Figure 5D. Because of the directionality of metal deposition and the different evaporation directions, different particle "shadows" corresponding to regions of uncoated substrates are observed for samples oriented at 30 and 45° (Figure 5D, left). Due to the anisotropy of the metal deposition and plasma etching, all fabricated structures share the same orientation within each sample. Plasma etching progressively reduces the symmetry of the fabricated structures by etching each semishell down to its dielectric core (Figure 5D, center and Figure 5D, right). Since the plasma etching direction is normal to the substrate, different etching patterns are ob-

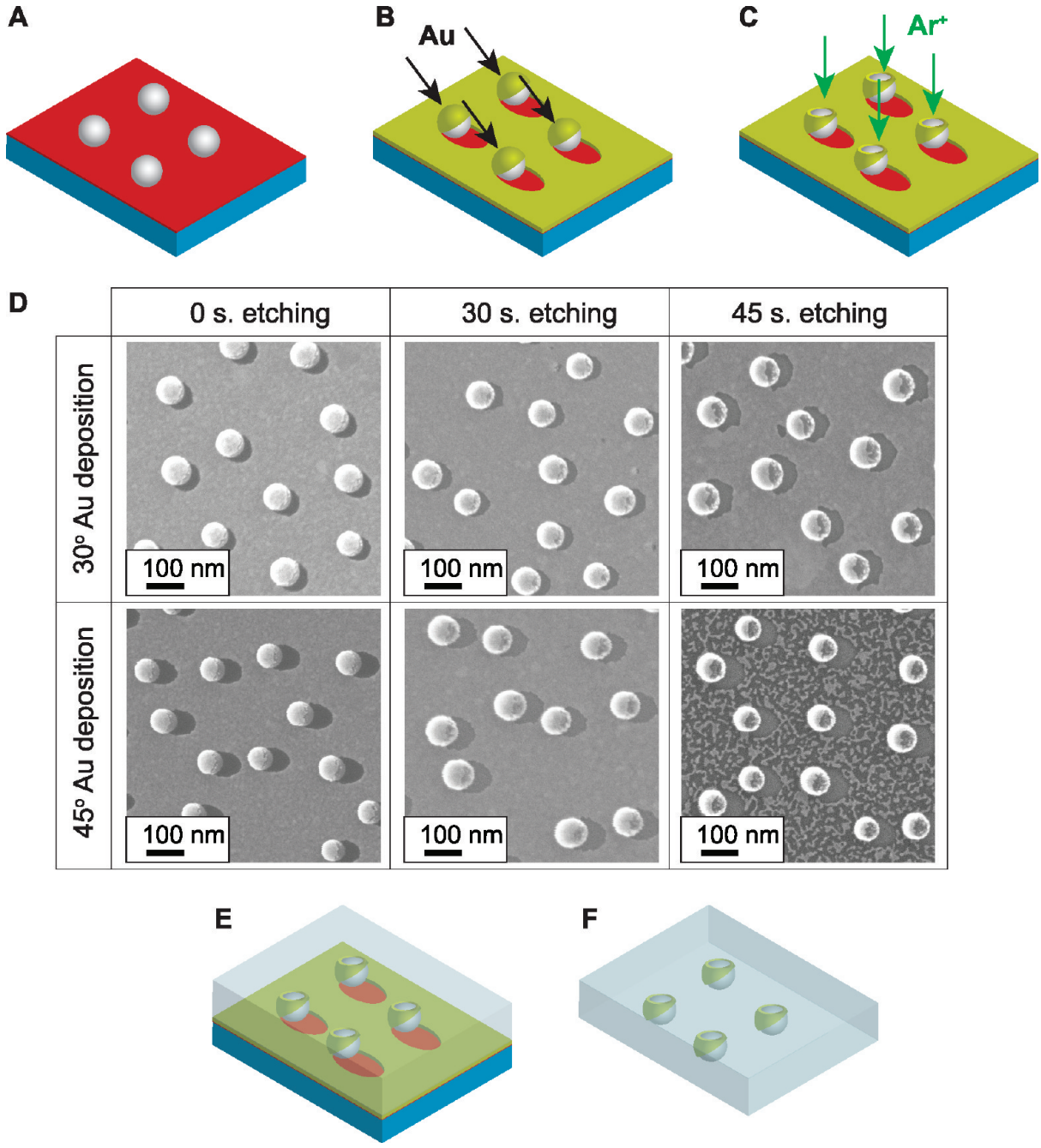

Figure 5. Fabrication of perforated Au semishells. (A) Patterning a functionalized substrate with polymer spheres. (B) Directional evaporation of Au at 30 or 45°. (C) Partial anisotropic etching of Au from the semicoated spheres using Ar^+ plasma. (D) SEM images for different etched nanocup samples prior to suspension in PDMS and separation from the substrate. (E) Embedding nanostructures into a PDMS matrix. (F) Separating the elastomer matrix with the suspended nanostructures from the substrate.

served for semishells fabricated using 30 and 45° evaporation angles. The Au film thickness deposited on angled surfaces decreases with increasing angle between the surface normal and the direction of the metal evaporation. For spherical beads, this determines the orientation of the deposited semishell on the substrate, with the center of the shell layer (thickest coating) facing the evaporation source. For an angled substrate, this results in a thinner flat Au layer on the substrate surrounding the fabricated semishell structures. In the etching process, the Au removal rate was the same for all samples used in the experiment. Due to differences in the surrounding film thicknesses, the thinner film is etched almost completely to the substrate (Figure 5D, bottom right), while thicker films remain continuous (Figure 5D, top right).

The etched semishells were separated from the substrate by coating the substrate with an elastomer, curing the elastomer layer, and peeling it from the substrate. Semishells removed in this way were embedded in an elastomer matrix, which preserved the angular orientation established during fabrication. The structures

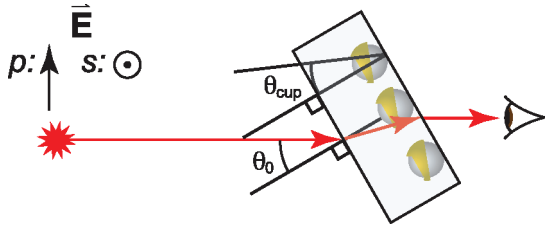

Figure 6. Schematic of the optical measurement of perforated semishell films, for P- and S-polarized light at a function of angle of incidence and etched semishell orientation. The incident beam refraction in the slab is illustrated.

form a relatively dense submonolayer; however, the interparticle separations were large enough that interparticle interactions could safely be neglected. The optical response of this film of semishells corresponds quite well to the optical response of the individual constituent nanostructures. The fabricated nanostructures were the semishells (Figure 5D, left), the semishells with one thinner etched side (Figure 5D, center), and the semishells with a hole (Figure 5D, right). The holes on the semishells were located off-axis due to the semishell orientation and the direction of etching. The holes had elliptical shapes as a result of the preferential etching of the thinner Au layer near the semishell edge. The extinction spectra of the fabricated nanostructures were collected according to the schematic in Figure 6 for two different polarizations and a range of incident angles (see Methods).

A reduced set of the collected spectra is shown in Figure 7A,C. To analyze these experimental results, we use single particle models for the films of Au semishells with and without perforations. The geometrical parameters of the particles were selected to match the SEM data shown in Figure 5D (see Supporting Information for the detailed comparison). In our theoretical analysis, the spherical cavity radius is 43 nm and the ellipsoidal Au shell radii are 57 and 68 nm. The hole introduced in this sample is elliptical, with major and minor radii 11.5 and 9.5 nm, respectively. The hole is placed off-axis by $\beta = 75°$, as defined in Figure 3A.

In Figure 7A,B, we show the extinction spectra for the case of a uniform semishell with no hole, as a function of angle of incident light for P-polarized excitation. Each curve represents a different external excitation effective angle of incidence (θ_{eff}) with respect to the semishell rotational axis, measured inside the elastomer slab and determined by Snell's law. At $\theta_{eff} = 0°$, the semishell is excited by a transverse-polarized external beam. In this case, the semishell supports a transverse dipole mode at wavelength $\lambda = 820$ nm. When the semishell is rotated 90°, it is excited by an axially polarized beam, exciting the semishell axial dipole mode at $\lambda = 628$ nm. We observe a very close agreement between the experimentally measured and calculated spectra.

In Figure 7C, we show the experimentally measured spectra of the semishells with an elliptical hole, obtained for a range of incident angles from 9°

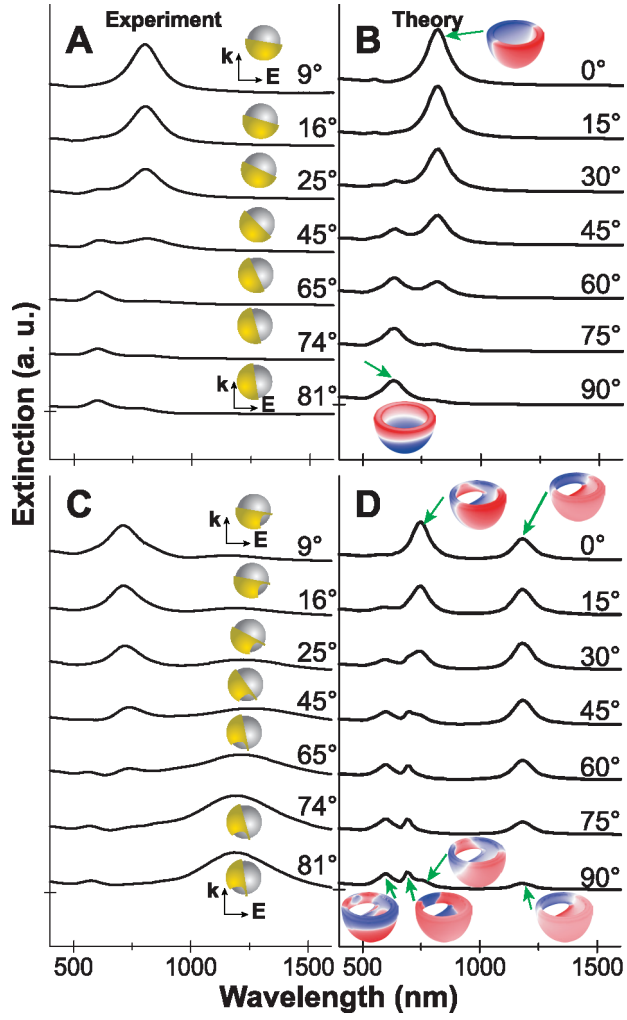

Figure 7. (A) Experimental and (B) theoretical extinction spectra of unperforated semishells. Semishells were fabricated with a Au deposition angle of 45°. (C) Experimental and (D) theoretical extinction spectra of perforated semishells. The theoretical calculations (B,D) include insets showing charge distributions at different wavelengths of incident light, indicated by arrows.

(transverse-polarized excitation) to 81° (axial-polarized excitation) using P-polarized incident light. The corresponding theoretical calculations are shown in Figure 7D for θ_{eff} ranging from 0 to 90°. As discussed in Figure 3, the symmetry breaking caused by the hole introduces dipole moments in the hybridized higher-order modes, making them visible in the spectra. As discussed previously, the introduction of a perforation into the metallic shell layer changes the topology of the structure such that it supports hybridized plasmon modes. In the case of transverse excitation ($\theta_{eff} = 0°$), we can see a clear plasmon hybridization[53,54] signature (described in further detail in the Supporting Information, Figure S5). The semishell transverse dipole mode at $\lambda = 820$ nm (Figure 7D, $\theta_{eff} = 0°$ case) hybridizes with the hole dipole mode, generating a bonding mode at $\lambda = 1180$ nm and an antibonding mode at $\lambda = 748$ nm. The intensity of the bonding mode has a maximum at the angle that aligns the **E**-field component of incident light

optimally with both the semishell opening and the plane of the hole. This angle is approximately 45° in the calculated spectrum and 74° in the measured spectrum. The bonding mode wavelength and relative amplitude are quite sensitive to hole size, shape, and position: for this reason, the peak is significantly broader in the experimental measurements since the slight variations between the fabricated structures in the film contribute significantly to the inhomogeneous broadening of the plasmon line widths.

With the development of more and more precise nanofabrication methods for making perforations into the metal layer of the semishell, this nanostructure has great potential as a general "platform" for the fabrication of a variety of nanostructures with different optical properties. Here we give two examples of how this structure could be modified in additional ways for specific applications as nanoscale optical components.

In Figure 8, we show how the introduction of a single or multiple holes onto a semishell can control the optical scattering pattern of the dipole mode. As we saw previously for offset holes, the presence of multiple perforations precisely reshapes the electric charge distribution and reroutes charge oscillations into mandated paths. In Figure 8A, we compare the optical response of three different theoretical models, a semishell with no perforation (black), a semishell with single hole (red), and a semishell with two holes (green). The incident wave has a transverse polarization with respect to the semishell structure. All holes are chosen to be elliptical cylindrical and not aligned with the incident field direction to represent a general case of reduced symmetry. In the two holes case, the two holes have different sizes, orientations, and elliptical profiles for better generality. Figure 8A shows that multiple holes leads to excitation of more higher-order modes and a red shift of the lowest energy bonding semishell mode. Because the presence of a single and multiple offset holes restricts the path of oscillating electrons, the light scattering pattern from the semishell is altered and dependent on the number of perforations (Figure 8B,C).

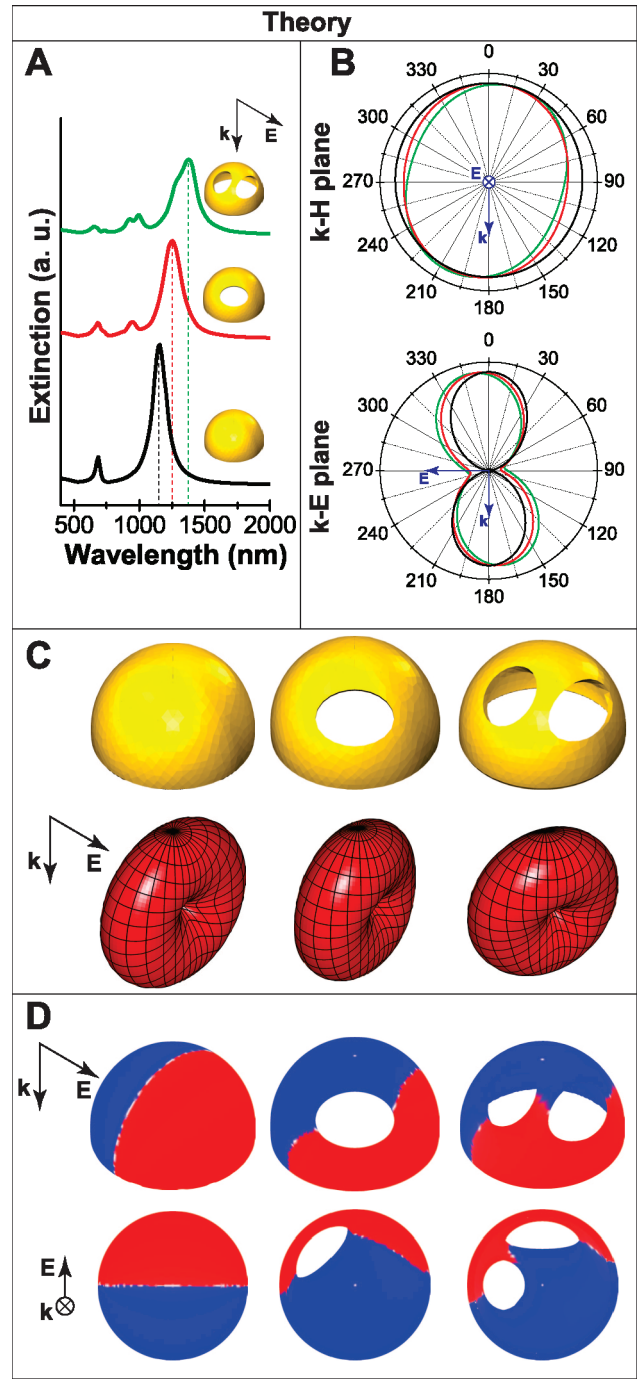

Figure 8. Simulated effect of the asymmetrically positioned elliptical holes on the optical response of a semishell. (A) Extinction spectra. (B) Normalized scattering in k−H and k−E planes at the strongest resonant peaks. (C) Geometry (top) and three-dimensional angular scattering distribution at the main resonance peaks (bottom) showing the dipole scattering profile modified by the presence of perforations in the semishell. (D) Induced surface charge distribution at the main resonance peaks showing the reshaping of the charge distribution due to the presence of the perforations in the semishell.

In Figure 8D, we compare the electric charge distribution for the transverse dipole mode of the three structures of Figure 8A. Regardless of hole placement on the semishell, the induced dipoles on the structure, as seen in the positive and negative charge distributions shown in Figure 8D, bisect the holes. As shown above for the case of an offset circular perforation, each hole provides an additional edge, altering the resonant plasmonic current. The extinction spectra are dominated by the bonding mode, for which the dipole of the primary semishell edge and the dipoles of the perforation edges hybridize to generate the largest possible dipole moment allowed by the curved geometry.

The ability to alter the angular distribution of the scattering spectrum by adding perforations onto this

semishell "nanoantenna" warrants a more comprehensive and broader study of this structure. The fabrication of precisely placed multiple perforations may ultimately provide a strategy for controlling light scattering by dictating the paths of the charge oscillations in individual nanostructures. Since the oscillation paths control the net dipole direction and magnitude, hole placement affects both the scattering direction and angular distribution.

The optical properties of a semishell can be modified even further by placing an elliptical cylindrical hole on the edge of the semishell, thus forming an edge defect in the form of an elliptical wedge-like slit (Figure 9A). This converts the semishell into a three-dimensional analogue of a split-ring resonator (SRR).[2−4,55] Here, the elliptical slit dimensions are defined from the top view by the slit depth (*D*) measured from the semishell edge and the slit width (*W*) measured at the semishell edge (the largest width of the slit). This structure supports both electric and magnetic modes. The electric mode is excited for transversely polarized **E**-field and does not require an inductive coupling to the structure. When the magnetic field is parallel to the semishell opening, there is no inductive coupling and only the electric mode can be excited. The magnetic mode can be excited when the incident magnetic field is normal to the semishell opening. For this excitation geometry, there is an inductive coupling between the incident magnetic field and the plasmon current of the semishell with the wedge-like slit. For both magnetic and electric excitations, the direction of the electric field is along the length of the elliptical slit. The geometries for electric and magnetic excitation of the respective modes are shown in Figure 9A. Figure 9B shows a comparison between the response of the semishell with a slit to the magnetic excitation (solid spectra) and to the electric excitation (dashed spectra) as functions of the excitation frequency. This comparison shows that the electric plasmon mode around 250 THz (only the low frequency tail is shown) in Figure 9B is excited in response to both the electric and magnetic excitation geometries. The magnetic mode around 150 THz is only excited for the magnetic excitation geometry (solid curves of Figure 9B). This magnetic mode frequency is sensitive to the slit shape and size. In order to show the tunability of the magnetic mode, we studied the effect of the slit width (*W*) in Figure 9B (left) and the effect of the slit depth (*D*) in Figure 9B (right).

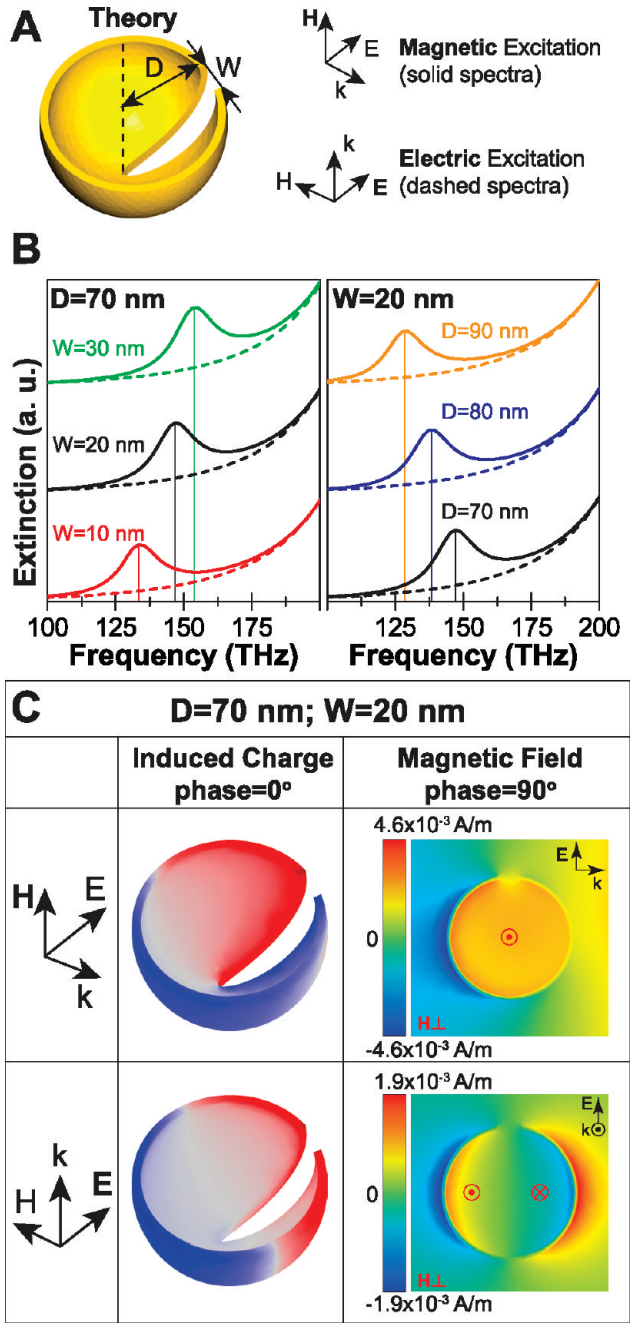

Figure 9. Simulated semishell with a wedge perforation as a split-ring resonator. (A) Schematic of the geometry and relative field orientation for magnetic and electric excitation with the same incident E-field polarization direction. (B) Extinction spectra of electric and magnetic excitations, showing the tunability of the magnetic mode due to the slit geometry. (C) Induced charge distributions at maximum charge separation, and the local magnetic field enhancement at the orthogonal phase.

To further investigate the difference between the electric and magnetic excitations, we analyze the induced surface charge and the magnetic field enhancement associated with the magnetic mode. Figure 9C shows the near-field properties in response to the magnetic excitation (top row) and the electric excitation (bottom row). The left column shows the local charge distribution at the maximum charge separation (phase = 0°), and the right column shows the local magnetic field component aligned with the semishell rotational axis at the maximum magnetic field enhancement

(phase = 90°). All plots are for ν = 147 THz, which corresponds to a wavelength of λ = 2 μm. In the case of magnetic excitation (top row), the electric charge distribution corresponds to the inductively driven oscillating current not accessible by electric field excitation alone. Consistent with this observation, the local magnetic field distribution (top right) shows an enhanced magnetic field uniformly distributed inside the semishell. For the electric excitation (bottom row) at the same frequency, the induced charge distribution corresponds to a weak off-resonant transverse semishell dipole mode aligned with the incident electric field (Figure 9C, bottom left). The local magnetic field distribution (bottom right) shows only a weak enhancement corresponding to a symmetric induced current oscillation on each side of the semishell.[46]

Semishells with wider and shorter slits support magnetic modes at higher frequencies (Figure 9B), which can be explained considering an LC resonance model of the structure. The metal body of the semishell acts as an inductor with nonzero series resistance due to the finite conductivity of the metal. The slit acts as the capacitor. The LC resonance frequency increases when the inductance or the capacitance decreases, by the well-known formula $\nu \sim (LC)^{-1/2}$. The primary effect of the slit width and depth is to change the effective capacitance, which decreases with increasing slit width (Figure 9B, left) and increases with increasing slit depth (lower resonance frequency in Figure 9B, right). The changes in the effective resistance and the effective inductance are negligible because the change in the metallic part of the structure is insignificant. The width of the resonance peak is proportional to the product of the effective high-frequency capacitance and the effective high-frequency resistance of the nanostructure, that is, the circuit time constant, and appears to be unchanged in the present parameter range.

CONCLUSION

We have designed a new class of plasmonic nanoparticles derived from metallic semishell particles by controlled perforation of their metallic shells. We have investigated the plasmon modes supported by this new geometry, their tunability, and the control of their amplitude as a function of reduced symmetry. These structures can be designed using theoretical models and fabricated using clean-room-based methods, resulting in films of semishells with optical properties in very good agreement with our theoretical calculations. The controlled perforation of the metallic shells can alter the far-field scattering properties and enable the excitation of magnetic plasmon modes in these structures.

METHODS

Etched Semishell Fabrication. Glass or silicon substrates were functionalized with poly(vinylpyridine) (PVP).[56] An aqueous suspension of Invitrogen (Sulfate Latex) or Bangs Laboratories' polystyrene spheres with a diameter of 90 nm was diluted with deionized water to 0.5% by mass. The substrates were placed in the colloidal suspension to form a submonolayer of isolated polymer spheres (Figure 5A) for 5−10 s, followed by careful rinsing with water and drying with nitrogen gas. The patterned substrates were mounted in an electron beam evaporator (Telemark) at angles of 30 and 45° between their normal and the direction of evaporation of the Au metal source. The adhesion layer of Ti (1 nm) followed by a 20 nm thick layer of Au was evaporated (Figure 5B). The samples were then placed flat in a Trion reactive ion etch (RIE) and etched for 30−45 s at 300 W RIE power and 100 sccm Ar flow under 80 Torr pressure. With this orientation, Au from the top of the angled semishells was partially removed (Figure 5C). Prior to PDMS immersion, each sample was imaged using JEOL-6500 scanning electron microscope (SEM). The substrates were immersed in Dow Corning Sylgard-184 polydimethylsiloxane (PDMS)[57] that was cured for 36 h at room temperature, embedding the semishells with a transparent matrix (Figure 5E). Subsequent removal of the PDMS layer separates the semishells from the Au-coated surface (Figure 5F).

Optical Characterization. Extinction data were measured using Cary 5000 UV−vis−NIR spectrophotometer with baseline subtraction. A blank PDMS slab with the same thickness as the samples was used to measure the baseline. The measurement schematic is shown in Figure 6. P- or S-polarized light was used. The orientation of the etched semishells is determined by two experimental angles: the angle between the nonetched cup axis and the substrate or suspending slab normal (θ_{cup}) and the angle of incidence of the probing beam to the suspending slab surface (θ_0) (see Figure 6). In this figure, the etched cup is shown with an assumption that etching occurs parallel to the substrate. However, due to the curved semishell surface and non-uniform thickness of the Au layer, the etched opening plane is not necessarily parallel to the substrate. The "axis" of the etched cup is assumed to be the same as that for the original nonetched cup. Using Snell's law with n_{PDMS} as the refractive index of the slab in Figure 6, the effective angle between the incident beam and the nonetched cup axis is $\theta_{eff} = \theta_{cup} - \sin^{-1}(\sin\theta_0/n_{PDMS})$. The experimental values of the effective angles are θ_{cup} = [30°, 45°] and θ_0 = [−60°, −45°, −30°, 0°, 30°, 45°, 60°].

Finite Element Modeling. The finite element method (FEM) is used to simulate the response of different semishell cases to external electromagnetic excitation. All FEM simulations are performed with the commercial software COMSOL 3.5a using scattered harmonic propagation (radio frequency module). The refractive index of the dielectric environment around the semishell, including the cavity, is chosen to match the elastomer matrix used in the experiment ($n^2 = \varepsilon$ = 2.13). To simulate the infinite space surrounding the nanoparticle, an absorbing layer is placed far enough to accommodate the largest value of the nanoparticle optical extinction cross section. The Au material is modeled using experimentally measured dielectric data with linear interpolation between the data points.[58] For the magnetic mode study in Figure 9, the Au material is modeled using a Drude model fit of the experimental data.[58] The Drude model provides the accurate description of the Au dielectric function below the interband transition (430 THz) and allows the extrapolation of the experimentally measured dielectric function to the range of frequencies lower than 155 THz. The Drude model fitting equation for the dielectric function is

$$\varepsilon(\nu) = \varepsilon_\infty - \frac{\nu_b^2}{\nu^2 + i\gamma\nu}$$

The fitting parameters are ε_∞ = 10.95 (background dielectric), γ = 18.69 THz (damping), and $\nu_b = 2.40 \times 10^3$ THz (bulk plasma frequency). Both the real and the complex part of the ex-

perimental dielectric function are fitted for the frequencies below the interband transition of Au (430 THz).

Surface Charge Evaluation on Metal−Dielectric Boundaries. Since the resonant charge oscillations do not necessarily coincide with the phase of the incident wave, the phase of the COMSOL solution has to be adjusted for the maximal induced surface charge amplitude. At any given phase, the surface charge boundary plot can be obtained by the following procedure.

In order to evaluate the surface charge on the metal−dielectric boundaries, Gauss theorem was applied to the **E**-field near the boundary to account for both bound and free surface charge densities.

$$\varepsilon_0 \iint_{\text{pill-box}} \vec{E}\cdot\vec{n}\,dS = \iint_{\text{metal-dielectric}} \sigma dS$$

The imaginary infinitely thin "pill-box" element is placed across the boundary, with the top surface in the dielectric and the bottom surface in metal. If the charge is located on the boundary only and the pill-box is infinitely thin, only the top and bottom surface contribute to the electric field flux integral on the left. The areas of the top and bottom surfaces in the left integral in the limit are equal to the area of the metal−dielectric boundary. Thus, the surface charge density is equal to the difference between the normal components of the electric field on the different sides of the metal−dielectric boundary.

$$\varepsilon_0\left(\iint_{\text{top}} \vec{n}\cdot\vec{E}\,dS + \iint_{\text{bottom}} \vec{n}\cdot\vec{E}\,dS\right) = \varepsilon_0\left(\iint_{\text{metal-dielectric}} \vec{n}_o\cdot\vec{E}_d\,dS + \iint_{\text{metal-dielectric}} -\vec{n}_o\cdot\vec{E}_m\,dS\right) = \iint_{\text{metal-dielectric}} \sigma dS$$

$$\sigma = \varepsilon_0\vec{n}_o\cdot(\vec{E}_d - \vec{E}_m)$$

COMSOL boundary expressions and boundary plots support up(<value>) and down(<value>) operators for the physical quantities, such as electric field, defined in domains above and below the boundary respectively.

$$\sigma = \varepsilon_0\vec{n}\cdot(\text{up}(\vec{E}) - \text{down}(\vec{E}))$$
$$\sigma = \varepsilon_0((\text{up}(E_x) - \text{down}(E_x))\cdot n_x + (\text{up}(E_y) - \text{down}(E_y))\cdot n_y + (\text{up}(E_z) - \text{down}(E_z))\cdot n_z)$$

The position of the upper and lower domain is determined by the normal vector direction set by the model, which is usually inconsistent among the multiple surfaces of the model. The overall expression for the surface charge density is invariant with respect to the normal definition since the opposite normal direction also switches up(<value>) and down(<value>) operators.

Acknowledgment. This work was supported by the Robert A. Welch Foundation grant C-1220 and C-1222, the Department of Defense National Security Science and Engineering Faculty Fellowship (N.J.H.), the Center for Advanced Solar Photophysics, an Energy Frontier Research Center funded by the U.S. Department of Energy, Office of Science, Office of Basic Energy Sciences, and the Air Force Office of Scientific Research (F49620-03-C-0068). Part of this work was supported by the Shared University Grid at Rice funded by NSF under Grant EIA-0216467, and a partnership between Rice University, Sun Microsystems, and Sigma Solutions, Inc. The authors thank K. Bao, R. Bardhan, L. Brown, R. Huschka, S. Mukherjee, J. Zuloaga, and Y. Wu for their valuable input, discussions, and proofreading of the manuscript.

Supporting Information Available: Detailed optical data compared to the FEM simulation for all experimental structures and different angles of incidence, induced surface charge distribution for the observed plasmon modes, and plasmon hybridization figure. This material is available free of charge *via* the Internet at http://pubs.acs.org.

REFERENCES AND NOTES

1. Giessen, H.; Vogelgesang, R. Glimpsing the Weak Magnetic Field of Light. *Science* **2009**, *326*, 529–530.
2. Husnik, M.; Klein, M. W.; Feth, N.; König, M.; Niegemann, J.; Busch, K.; Linden, S.; Wegener, M. Absolute Extinction Cross-Section of Individual Magnetic Split-Ring Resonators. *Nat. Photonics* **2008**, *2*, 614–617.
3. Soukoulis, C. M.; Linden, S.; Wegener, M. Negative Refractive Index at Optical Wavelengths. *Science* **2007**, *315*, 47–49.
4. Linden, S.; Enkrich, C.; Wegener, M.; Zhou, J. F.; Koschny, T.; Soukoulis, C. M. Magnetic Response of Metamaterials at 100 Terahertz. *Science* **2004**, *306*, 1351–1353.
5. Xiao, S. M.; Chettiar, U. K.; Kildishev, A. V.; Drachev, V. P.; Shalaev, V. M. Yellow-Light Negative-Index Metamaterials. *Opt. Lett.* **2009**, *34*, 3478–3480.
6. Xiao, S. M.; Chettiar, U. K.; Kildishev, A. V.; Drachev, V.; Khoo, I. C.; Shalaev, V. M. Tunable Magnetic Response of Metamaterials. *Appl. Phys. Lett.* **2009**, *95*, 033115.
7. Ozbay, E. Plasmonics: Merging Photonics and Electronics at Nanoscale Dimensions. *Science* **2006**, *311*, 189–193.
8. Bozhevolnyi, S. I.; Volkov, V. S.; Devaux, E.; Laluet, J.-Y.; Ebbesen, T. W. Channel Plasmon Subwavelength Waveguide Components Including Interferometers and Ring Resonators. *Nature* **2006**, *440*, 508–511.
9. Zia, R.; Schuller, J. A.; Chandran, A.; Brongersma, M. L. Plasmonics: The Next Chip-Scale Technology. *Mater. Today* **2006**, *9*, 20–27.
10. Holmgaard, T.; Chen, Z.; Bozhevolnyi, S. I.; Markey, L.; Dereux, A.; Krasavin, A. V.; Zayats, A. V. Bend- and Splitting Loss of Dielectric-Loaded Surface Plasmon-Polariton Waveguides. *Opt. Express* **2008**, *16*, 13585–13592.
11. Kim, J. T.; Ju, J. J.; Park, S.; Kim, M.-S.; Park, S. K.; Lee, M.-H. Chip-to-Chip Optical Interconnect Using Gold Long-Range Surface Plasmon Polariton Waveguides. *Opt. Express* **2008**, *16*, 13133–13138.
12. Dionne, J. A.; Diest, K.; Sweatlock, L. A.; Atwater, H. A. Plasmostor: A Metal-Oxide-Si Field Effect Plasmonic Modulator. *Nano Lett.* **2009**, *9*, 897–902.
13. Akimov, Y. A.; Koh, W. S.; Ostrikov, K. Enhancement of Optical Absorption in Thin-Film Solar Cells through the Excitation of Higher-Order Nanoparticle Plasmon Modes. *Opt. Express* **2009**, *17*, 10195–10205.
14. Catchpole, K. R.; Polman, A. Design Principles for Particle Plasmon Enhanced Solar Cells. *Appl. Phys. Lett.* **2008**, *93*, 191113.
15. Large, N.; Saviot, L.; Margueritat, J.; Gonzalo, J.; Afonso, C. N.; Arbouet, A.; Langot, P.; Mlayah, A.; Aizpurua, J. Acousto-Plasmonic Hot Spots in Metallic Nano-Objects. *Nano Lett.* **2009**, *9*, 3732–3738.
16. Pillai, S.; Catchpole, K. R.; Trupke, T.; Green, M. A. Surface Plasmon Enhanced Silicon Solar Cells. *J. Appl. Phys.* **2007**, *101*, 093105.
17. Schnell, M.; García-Etxarri, A.; Huber, A. J.; Crozier, K.; Aizpurua, J.; Hillenbrand, R. Controlling the Near-Field Oscillations of Loaded Plasmonic Nanoantennas. *Nat. Photonics* **2009**, *3*, 287–291.
18. Wahsheh, R. A.; Lu, Z. L.; Abushagur, M. A. G. Nanoplasmonic Couplers and Splitters. *Opt. Express* **2009**, *17*, 19033–19040.
19. Zhang, Q.; Huang, X.-G.; Lin, X.-S.; Tao, J.; Jin, X.-P. A Subwavelength Coupler-Type Mim Optical Filter. *Opt. Express* **2009**, *17*, 7549–7554.
20. Atwater, H. A.; Polman, A. Plasmonics for Improved Photovoltaic Devices. *Nat. Mater.* **2010**, *9*, 205–213.
21. Kwon, M.-K.; Kim, J.-Y.; Kim, B.-H.; Park, I.-K.; Cho, C.-Y.; Byeon, C. C.; Park, S.-J. Surface-Plasmon-Enhanced Light-Emitting Diodes. *Adv. Mater.* **2008**, *20*, 1253–1257.
22. Slavík, R.; Homola, J. Optical Multilayers for LED-Based Surface Plasmon Resonance Sensors. *Appl. Opt.* **2006**, *45*, 3752–3759.
23. Okamoto, K.; Vyawahare, S.; Scherer, A. Surface-Plasmon Enhanced Bright Emission from CdSe Quantum-Dot Nanocrystals. *J. Opt. Soc. Am. B: Opt. Phys.* **2006**, *23*, 1674–1678.
24. Yeh, D.-M.; Huang, C.-F.; Chen, C.-Y.; Lu, Y.-C.; Yang, C. C. Localized Surface Plasmon-Induced Emission Enhancement of a Green Light-Emitting Diode. *Nanotechnology* **2008**, *19*, 345201.

25. Okamoto, K.; Niki, I.; Shvartser, A.; Narukawa, Y.; Mukai, T.; Scherer, A. Surface-Plasmon-Enhanced Light Emitters Based on InGaN Quantum Wells. *Nat. Mater.* **2004**, *3*, 601–605.
26. Stuart, H. R.; Hall, D. G. Island Size Effects in Nanoparticle-Enhanced Photodetectors. *Appl. Phys. Lett.* **1998**, *73*, 3815–3817.
27. Oldenburg, S. J.; Averitt, R. D.; Westcott, S. L.; Halas, N. J. Nanoengineering of Optical Resonances. *Chem. Phys. Lett.* **1998**, *288*, 243–247.
28. Wang, H.; Brandl, D. W.; Le, F.; Nordlander, P.; Halas, N. J. Nanorice: A Hybrid Plasmonic Nanostructure. *Nano Lett.* **2006**, *6*, 827–832.
29. Hu, Y.; Noelck, S. J.; Drezek, R. A. Symmetry Breaking in Gold−Silica−Gold Multilayer Nanoshells. *ACS Nano* **2010**, *4*, 1521–1528.
30. Tassin, P.; Zhang, L.; Koschny, T.; Economou, E. N.; Soukoulis, C. M. Low-Loss Metamaterials Based on Classical Electromagnetically Induced Transparency. *Phys. Rev. Lett.* **2009**, *102*, 053901.
31. Knight, M. W.; Grady, N. K.; Bardhan, R.; Hao, F.; Nordlander, P.; Halas, N. J. Nanoparticle-Mediated Coupling of Light into a Nanowire. *Nano Lett.* **2007**, *7*, 2346–2350.
32. Ditlbacher, H.; Hohenau, A.; Wagner, D.; Kreibig, U.; Rogers, M.; Hofer, F.; Aussenegg, F. R.; Krenn, J. R. Silver Nanowires as Surface Plasmon Resonators. *Phys. Rev. Lett.* **2005**, *95*, 257403.
33. Park, T.-H.; Mirin, N.; Lassiter, J. B.; Nehl, C. L.; Halas, N. J.; Nordlander, P. Optical Properties of a Nanosized Hole in a Thin Metallic Film. *ACS Nano* **2008**, *2*, 25–32.
34. Park, T.-H.; Nordlander, P. On the Nature of the Bonding and Antibonding Metallic Film and Nanoshell Plasmons. *Chem. Phys. Lett.* **2009**, *472*, 228–231.
35. Penninkhof, J. J.; Moroz, A.; Van Blaaderen, A.; Polman, A. Optical Properties of Spherical and Oblate Spheroidal Gold Shell Colloids. *J. Phys. Chem. C* **2008**, *112*, 4146–4150.
36. Wang, H.; Wu, Y. P.; Lassiter, B.; Nehl, C. L.; Hafner, J. H.; Nordlander, P.; Halas, N. J. Symmetry Breaking in Individual Plasmonic Nanoparticles. *Proc. Natl. Acad. Sci. U.S.A.* **2006**, *103*, 10856–10860.
37. Mirin, N. A.; Halas, N. J. Light-Bending Nanoparticles. *Nano Lett.* **2009**, *9*, 1255–1259.
38. Preston, T. C.; Signorell, R. Growth and Optical Properties of Gold Nanoshells Prior to the Formation of a Continuous Metallic Layer. *ACS Nano* **2009**, *3*, 3696–3706.
39. Wu, D. J.; Liu, X. J. Influence of Spherically Anisotropic Core on the Optical Properties of Gold Nanoshell. *Appl. Phys. A: Mater. Sci. Process.* **2009**, *94*, 537–541.
40. Mulvihill, M. J.; Ling, X. Y.; Henzie, J.; Yang, P. D. Anisotropic Etching of Silver Nanoparticles for Plasmonic Structures Capable of Single-Particle SERS. *J. Am. Chem. Soc.* **2010**, *132*, 268–274.
41. Ye, J.; Lagae, L.; Maes, G.; Borghs, G.; Van Dorpe, P. Symmetry Breaking Induced Optical Properties of Gold Open Shell Nanostructures. *Opt. Express* **2009**, *17*, 23765–23771.
42. Cortie, M.; Ford, M. A Plasmon-Induced Current Loop in Gold Semi-Shells. *Nanotechnology* **2007**, *18*, 235704.
43. Lassiter, J. B.; Knight, M. W.; Mirin, N. A.; Halas, N. J. Reshaping the Plasmonic Properties of an Individual Nanoparticle. *Nano Lett.* **2009**, *9*, 4326–4332.
44. Maaroof, A. L.; Cortie, M. B.; Harris, N.; Wieczorek, L. Mie and Bragg Plasmons in Subwavelength Silver Semi-Shells. *Small* **2008**, *4*, 2292–2299.
45. Ye, J.; Van Dorpe, P.; Van Roy, W.; Lodewijks, K.; De Vlaminck, I.; Maes, G.; Borghs, G. Fabrication and Optical Properties of Gold Semishells. *J. Phys. Chem. C* **2009**, *113*, 3110–3115.
46. Hao, F.; Larsson, E. M.; Ali, T. A.; Sutherland, D. S.; Nordlander, P. Shedding Light on Dark Plasmons in Gold Nanorings. *Chem. Phys. Lett.* **2008**, *458*, 262–266.
47. Larsson, E. M.; Alegret, J.; Käll, M.; Sutherland, D. S. Sensing Characteristics of NIR Localized Surface Plasmon Resonances in Gold Nanorings for Application as Ultrasensitive Biosensors. *Nano Lett.* **2007**, *7*, 1256–1263.
48. Kim, S.; Jung, J. M.; Choi, D. G.; Jung, H. T.; Yang, S. M. Patterned Arrays of Au Rings for Localized Surface Plasmon Resonance. *Langmuir* **2006**, *22*, 7109–7112.
49. Aizpurua, J.; Hanarp, P.; Sutherland, D. S.; Käll, M.; Bryant, G. W.; García de Abajo, F. J. Optical Properties of Gold Nanorings. *Phys. Rev. Lett.* **2003**, *90*, 057401.
50. Hao, F.; Nordlander, P.; Burnett, M. T.; Maier, S. A. Enhanced Tunability and Linewidth Sharpening of Plasmon Resonances in Hybridized Metallic Ring/Disk Nanocavities. *Phys. Rev. B: Condens. Matter* **2007**, *76*, 245417.
51. Jung, K.-Y.; Teixeira, F. L.; Reano, R. M. Au/Sio_2 Nanoring Plasmon Waveguides at Optical Communication Band. *J. Lightwave Technol.* **2007**, *25*, 2757–2765.
52. Shumaker-Parry, J. S.; Rochholz, H.; Kreiter, M. Fabrication of Crescent-Shaped Optical Antennas. *Adv. Mater.* **2005**, *17*, 2131–2134.
53. Prodan, E.; Radloff, C.; Halas, N. J.; Nordlander, P. A Hybridization Model for the Plasmon Response of Complex Nanostructures. *Science* **2003**, *302*, 419–422.
54. Prodan, E.; Nordlander, P. Plasmon Hybridization in Spherical Nanoparticles. *J. Chem. Phys.* **2004**, *120*, 5444–5454.
55. Walther, M.; Ortner, A.; Meier, H.; Löffelmann, U.; Smith, P. J.; Korvink, J. G. Terahertz Metamaterials Fabricated by Inkjet Printing. *Appl. Phys. Lett.* **2009**, *95*, 251107.
56. Malynych, S.; Luzinov, I.; Chumanov, G. Poly(vinyl pyridine) as a Universal Surface Modifier for Immobilization of Nanoparticles. *J. Phys. Chem. B* **2002**, *106*, 1280–1285.
57. Malynych, S.; Robuck, H.; Chumanov, G. Fabrication of Two-Dimensional Assemblies of Ag Nanoparticles and Nanocavities in Poly(dimethylsiloxane) Resin. *Nano Lett.* **2001**, *1*, 647–649.
58. Johnson, P. B.; Christy, R. W. Optical-Constants of Noble-Metals. *Phys. Rev. B: Condens. Matter* **1972**, *6*, 4370–4379.